Journal of Alloys and Compounds 965 (2023) 171290

Contents lists available at ScienceDirect

Journal of Alloys and Compounds

journal homepage: www.elsevier.com/locate/jalcom

# A comprehensive study on microstructure, *in-vitro* biodegradability, bacterial sensitivity, and cellular interactions of novel ternary Zn-Cu-xAg alloys for urological applications

H. Yilmazer [a,b,*], S. Basit [c], A. Sen [a], Y. Yilmazer [d], B. Dalbayrak [e], E.D. Arisan [e], S. Arisan [f], R.K. Islamgaliev [g], B. Dikici [h,**]

[a] Yildiz Technical University, Department of Metall. and Materials Engineering, Istanbul 34220, Turkiye
[b] Yildiz Technical University, Health Biotechnology Joint Research and Application Center of Excellence, 34220 Esenler, Istanbul, Turkiye
[c] Kırşehir Ahi Evran University, Department of Mechanical Engineering, Kirsehir 40100, Turkiye
[d] Sabahattin Zaim University, Department of Molecular Biology and Genetics, Istanbul 34300, Turkiye
[e] Gebze Technical University, Institute of Biotechnology, Kocaeli 41400 Turkiye
[f] University of Health Sciences, Hamidiye Etfal Research and Training Hospital, Istanbul 34668, Turkiye
[g] Ufa University of Science and Technology, Institute for Physics of Advanced Mater., Ufa 450076, Russia
[h] Atatürk University, Department of Metallurgical and Materials Engineering, Erzurum 25240, Turkiye

ARTICLE INFO

*Keywords:*
Bioabsorbable
Zn-Cu-Ag alloy
Urological devices
Degradation
In-vitro corrosion
Cell culture

ABSTRACT

Novel ternary Zn-Cu-xAg alloys are designed and fabricated by the casting method under a vacuum atmosphere and then homogenized at 350 °C for 15 h. The effect of Ag concentration (x: 0, 1, 2, 3, and 4 wt%) on microstructure, hardness, in vitro corrosion, biodegradability, and bacterial sensitivity was studied systematically. The structural analysis of the alloys was investigated by using a scanning electron microscope (SEM-EDS), and an optical microscope (OM). Besides, phase characterization of the samples was conducted using X-ray diffraction (XRD). The degradation behaviors of the alloys were determined under in vitro conditions, electrochemical polarization, and immersion tests (up to 21 days) in artificial urine (AU) solution. The maximum hardness value for Zn-1Cu-4Ag alloy was about 2.38 times higher than pure Zn due to solid-solution strengthening and precipitation hardening of (Ag, Cu)$Zn_4$ phases. The highest and lowest $I_{corr}$ values, reference also corrosion rate, were calculated in Zn-1Cu and Zn-1Cu-3Ag alloys as 17.13 and 1.318 mA·cm$^{-2}$, respectively. The alloys' bacterial sensitivities were evaluated with the disc diffusion test for *E. coli* and *S. aureus*. The inhibition ratio of the Zn-1Cu-1Ag was higher than the inhibition rates of the other alloys on *E. coli* and *S. aureus*. In addition, the biological properties of the generated material were promising by altering cell survival/death ratio in both prostate epithelial and bladder cancer cells related to their use potential in urology.

## 1. Introduction

Biodegradable metallic implant materials are a relatively new area of research and development in biomedical engineering. These materials are designed to be absorbed by the human body over time, eliminating the need for a second surgical operation to remove the implant. The main advantage of these materials is that they reduce the risk of implant-related complications and provide a more natural healing process [1,2]. Recent studies showed that the most popular biodegradable materials are Fe, Mg, and Zn metals and their alloys. Several clinical studies have evaluated the performance of biodegradable (or bioresorbable) metallic implants, and the results have been encouraging [3,4]. The time-dependent degradation of these materials is promising to reduce implant-based problems on the tissue site. However, the degradation time may vary between patients according to disease or metabolic conditions. If the implant degrades before the tissue regeneration, it may not provide adequate support for the surrounding tissue, leading to failure. On the other hand, if it takes too long to degrade, it may cause discomfort or irritation for the patient [5].

The urinary tract is susceptible to various clinical problems such as

* Corresponding author at: Yildiz Technical University, Department of Metall. and Materials Engineering, Istanbul 34220, Turkiye.
** Corresponding author.
*E-mail addresses:* hakanyil@yildiz.edu.tr (H. Yilmazer), burakdikici@gatauni.edu.tr (B. Dikici).

https://doi.org/10.1016/j.jallcom.2023.171290
Received 22 February 2023; Received in revised form 27 May 2023; Accepted 5 July 2023
Available online 10 July 2023

blockage or obstruction and injuries, which present an economic and societal burden worldwide. A urinary tract obstruction can occur at any part of the urinary system, such as the ureter, which connects the kidneys to the bladder. The human ureters are essential to tissue that connects the kidney and the bladder and plays a role in evacuating urinary fluid. Urological diseases like kidney stones and retroperitoneal tumors can cause obstruction of the approximately 4 mm in diameter and 30 cm in length tubular structure of soft ureter tissues, leading to kidney failure and other complications [6].

For over a century, urological practitioners have widely utilized ureteral stents to bypass obstructions and reinstate urine flow in the upper urinary tract, but patient discomfort, crusting, and permanent stent-related infection (biofilm formation, lower urinary tract symptoms, hematuria) are frequently encountered. In addition, general anesthesia is typically necessary in pediatric cases, and a second operation is required to remove the stent [7]. Biodegradable metallic materials can be a unique alternative to solve these problems.

An ideal material for urological tissue applications should be able to reduce bacterial colonization and provide a healthy environment for the neighbor cells while being degradable in the body [6]. The degraded material should be beneficial in the future time to release therapeutics. Due to their biocompatibility and mechanical benefits, Fe and Mg alloys have been extensively investigated as degradable materials for medical applications [8–11]. However, it was observed during the studies that besides these advantages, there are some functional deficiencies and a low degradation rate of Fe or causing the formation of $H_2$ gas cavities of Mg alloys in vivo [12–16].

In recent years, Zn-based alloys have garnered more interest as a potential alternative. The advantages of Zn include a corrosion rate that falls between that of Mg and Fe, no generation of hydrogen gas during degradation, ease of fabrication due to its low melting temperature, and low reactivity during melting [17]. Pure Zn does not possess the required mechanical properties for stent applications, thus requiring alloying. Numerous research groups investigating alternative biodegradable materials have studied various alloying elements, such as Mg, Ca, Sr, Fe, and Mn, to enhance the mechanical properties of Zn [18–24]. The studies reported mechanical instability for Zn-based alloys due to low thermal stability and self-aging [25].

To mimic the potential effects of biodegradable materials, cell culture tests are critical to evaluate the undesired outcomes of the materials. On other side, the biocompatibility of alloy material is crucial to understand the biological responses in related tissue sites. The morphological properties of the cells on the material are definitive to evaluate the adhesive characteristics of cell lines. Additionally, the cell viability of seeded cells on or near the side of the material in the same Petri dish is exemplary [26].

In the search for a suitable biodegradable material for cardiovascular stent applications, Zn-based alloys have been widely investigated [27]. Of these alloys, the Zn-Cu binary alloy has been systematically studied by Niu et al. [28] and Tang et al. [29], with promising results due to its good mechanical properties, high thermal stability, and self-aging resistance resulting from solid solution strengthening. Because of the high solubility of Cu in Zn, almost all of the Cu atoms dissolve in the Zn if Cu in Zn has 1 wt%. Furthermore, Sikora-Jasinska et al. [30] demonstrated that adding the Ag element to Zn-based alloys could improve their yield strength and ultimate tensile strength values. For instance, the Zn-1.5 Cu-1.5 Ag alloy displayed better cell viability than both the negative control group and pure Zn, particularly after 1-day and 3-day cultures [31]. In another study, biodegradable Zn-Cu-0.5Ag and Zn-Cu-1.0Ag Ag alloying were studied by Di et al. [32] for their microstructure, corrosion behavior, mechanical features, and antibacterial capabilities. The study demonstrated that as the Ag concentration in the Zn-Cu master alloy increased, the average grain size of the alloys decreased. When compared to Zn-1Cu-0.5Ag alloy, Zn-1Cu-1Ag showed higher ductility, hardness, and ultimate tensile strength as a result of the grain refining effect. Additionally, Zn-1Cu-1Ag alloy showed effective anti-bacterial properties and a mild deterioration rate of 0.0484 mm/year, which made it suitable for orthopedic applications. Jin et al. [33] investigated the effects of the Ag content on the microstructure and mechanical characteristics of the Zn-1.5Cu-xAg-0.1Zr (x: 0, 0.1, 0.5, and 1.0) alloy. The mechanical properties of the alloys were significantly improved with the increasing Ag ratio in the master alloy, as well as the alloys' yield and ultimate tensile strength was increased due to precipitated $AgZn_3$ phases in the microstructure. Thus, the Zn-Cu alloy, with the addition of the Ag element, can be considered a suitable candidate for a urethral stent.

The degradation rate of biodegradable materials is critical for consistency with the surrounding tissue's healing process. However, further research is needed to evaluate these materials' long-term performance and safety fully. By the way, although the Zn-xCu alloys for stent applications were detailly researched in the literature, systematic investigations directly on biodegradable Zn-1Cu-xAg alloys are very limited. Thus, novel ternary Zn-1Cu-xAg alloys are designed and fabricated by the casting method in this study. The effect of Ag concentration (x: 0, 1, 2, 3, and 4 wt%) on microstructure, hardness, in vitro corrosion, biodegradability, and bacterial sensitivity was studied systematically.

## 2. Experimental methods

### 2.1. Fabrication of alloys

In this study, biodegradable Zn-1Cu-xAg (x: 0, 1, 2, 3, and 4 wt%) alloys were fabricated by the casting method. For this purpose, 99.99% pure Zn (CAS: 7440–66–6), Cu (CAS: 7440–50–8), and Ag (CAS: 7440–22–4) were used to prepare the alloys. The elements were melted at 550 °C in a vacuum atmosphere to prevent oxidation of the alloys using a high-purity graphite crucible. The melting process was repeated by three times by reversing the poured bar to maintain homogeneous distribution of the alloys. The final molten alloys were poured into a preheated (270 °C) steel mold to obtain metal bars of 15 mm diameter and 100 mm length. Finally, a homogenization heat treatment was applied to the bars at 350 °C for 15 h followed by the quenching. The alloys were cut using wire-cutting machining for the preparation of samples. The sample surfaces were ground (up to #2000 abrasive paper), and polished with diamond suspensions of 3, 1, and 0.25 μm, respectively. The samples were etched with % 2 HCl solutions for the microstructural characterizations.

### 2.2. Biodegradation analysis with in-vitro immersion tests

The samples were ultrasonically cleaned in ethanol and then sterilized under UV radiation (a wavelength of 365 nm) for 1 h before the immersion tests. The tests were conducted with artificial urine (AU) solution, whose chemical composition is similar to healthy human urine. The composition of the AU solution is also given in Table 1. The preparation of the AU solution was described in ref. [34]. The equipment used in AU solution preparation has been sterilized by washing it with alcohol. Ultrapure water was heated to 37 °C with continuous stirring with a magnetic stirrer. The reagents in Table 1 were added and dissolved in ultrapure water respectively. The AU solution was balanced at

**Table 1**
Reagents for preparing a 1 L of the synthetic urine [31].

| Reagents | Amount ($g{\cdot}L^{-1}$) |
|---|---|
| Diammonium phosphate $(NH_4)_2HPO_4$ | 1.70 |
| Calcium chloride ($CaCl_2$) | 0.24 |
| Magnesium chloride hexahydrate ($MgCl_2{\cdot}6\ H_2O$) | 0.50 |
| Potassium chloride (KCl) | 2.02 |
| Sodium sulfate ($Na_2SO_4$) | 2.02 |
| Urea | 0.76 |
| Creatine | 1.50 |
| Uric Acid | added until reaches a pH of 7 |

a pH of 7.0 using uric acid. Firstly, the initial weight of each sample was measured for further calculations. The surface area of the samples was calculated and the AU solution of approximately 20 mL/cm$^2$ was used during the tests [35]. The samples were subjected to the immersion tests in the AU solution at 37 °C up to 21 days. The AU solution was refreshed every 48 h without any change in the position of the samples. The samples were washed using a chromium oxide solution (200 g·L$^{-1}$) to remove corrosion products before measuring the final weight after the immersion tests.

### 2.3. Microstructural characterization

Microstructures of the alloys were observed using an optical microscope (OM) integrated with a digital camera with image analysis techniques (NIS-Elements Version 4.3). The phase composition of the samples was conducted by X-ray diffraction (XRD, Bruker Discovery D8) having a Cu Ka (a wavelength of 1,54 A) radiation source at an operating voltage of 35 kV and a tube current of 40 mA. Besides, the inductively coupled plasma mass spectrometry (ICP-MS, Agilent Technologies 7700x) method was used to determine the precise composition of all produced alloys.

### 2.4. In-vitro electrochemical corrosion tests

The electrochemical potentiodynamic scanning (PDS) tests were applied to the samples by using a potentiostat/galvanostat (Gamry, PCII4/750) at body temperature (37 ± 0.5 °C). AU solution was used as an electrolyte to mimic the urinary environment during the tests. Tests were carried out according to the three-electrode technique within 400 mL volume electrolyte. A Pt wire electrode and an Ag/AgCl electrode were used as a counter, and a reference, respectively. The open circuit potential (OCP) changes for stabilizing the alloy surfaces with electrolytes were monitored before the potentiodynamic scanning (PDS) tests. After equilibrium, the scanning was started on the alloys from − 0.3 V vs OCP value and continued the anodic side with a 1 mV·s$^{-1}$ scan rate. Besides, surface observations before and after the corrosion test were carried out using a scanning electron microscope (SEM, Hitachi TM-1000) attached electron dispersive spectroscope (EDS).

### 2.5. Hardness tests

The hardness values of the samples were measured with a Vickers hardness (HV) machine under a load of 1000 gf for a dwell duration time of 15 s at room temperature. The average hardness values of the alloys were calculated using 10 individual values taken from the random points of the sample surface. During the hardness tests of Ag added Zn-1Cu alloys, by covering an adequate number of grains with the hardness indent, we aimed to capture a representative sample of the material's microstructure. Thus, the indenter load magnitude was set in a way that the indenters' trace covered at least 10 grains.

### 2.6. Bacterial sensitivity tests

The antibacterial activity of the alloys was determined using the disc diffusion test [36]. In order to achieve the appropriate bacterial density, suspensions of *E. coli* (ATCC 25922) and *S. aureus* (ATCC 25923) were taken from 18-hour nutritional broth cultures and modified to 0.5 McFarland standard density (1.5 ×10$^8$ CFU·mL$^{-1}$). 0.1 mL of the bacterial suspensions (1.5 ×10$^6$ CFU·mL$^{-1}$) were used to inoculate Mueller-Hinton agar plates. The samples were sterilized for 30 min under UV light with a wavelength of 254 nm after being washed in an ultrasonic bath for 3 min with water and ethyl alcohol. The test samples were prepared and then put on Petri dishes with bacterium plates. A digital micrometer was used to measure the inhibition zone surrounding the discs after the plates were incubated at 37 °C for 24 h [37]. Different groups were formed to select the best samples, and tests were carried out three times.

### 2.7. Determination of cell survival and death

The samples were taken under the Class II Laminar flow before UV sterilization for 30 min before cell culture studies. After sterilization, samples were placed onto the 24-well plate. Normal prostate epithelial cells (PNT1A) (ECACC 95012614), and human urinary bladder cancer cells (T24) (ATCC HTB-4) were grown with DMEM high glucose with 4.5 g·L$^{-1}$ D-Glucose, L-Glutamine, and sodium pyruvate (NutriCulture, Ecobiotech) medium supplemented with 10% Fetal Bovine Serum (Gibco) and 1% penicillin-streptomycin (PAN Biotech) in a humidified CO2 incubator (Thermo). When cells reached 80% confluency, cells were detached with trypsin/EDTA and counted with Haemocytometer (Marienfield). After 5 min of centrifugation at 1500 rpm, the cell pellet was dissolved with the appropriate amount of DMEM to obtain 28.000 cells/well for the 24-well plate and 10.000 cells/well for the 96-well plate for PNT1A and T24, respectively. The dissolved cells were seeded onto the material with a seeding volume of 1 mL per well for PNT1A prostate epithelial cells and 300 μL per well for T24 urothelial cancer cells. Moreover, the seeding was examined directly to the top of the samples and the cells were incubated for 48 h under the same conditions with growth. After 48 h incubation, the existing medium was removed with a staining medium, including serum- and antibiotic-free DMEM, 4 nM DiOC6 (3,3′-Dihexyloxacarbocyanine Iodide) (Thermo Fisher) for living cells examination, and 2 mg/mL Propidium Iodine (PI) (Sigma-Aldrich) to identify dead cells. Then, 15 min of incubation at 37 °C with 5% CO2 was applied, and the fluorescence images were taken at a ZOE Fluorescence cell imager (BioRad) with the relevant excitation and emission wavelengths.

### 2.8. Statistical analysis

The samples were analyzed with a one-way ANOVA test and independent-sample t-tests were used to describe significant differences between samples. Results were presented as mean ± standard deviation. The level of significance was selected as $p < 0.05$.

## 3. Results and discussion

This study was organized mainly in two parts. In the first part, fabrication, microstructure, hardness, and in-vitro degradation behaviors of the alloys were performed and evaluated. In the second part of the study, bacterial sensitivity, cell survival, and death of the alloy's surfaces were researched and determined.

### 3.1. Microstructure

ICP-MS analysis of the produced alloys' composition revealed that the alloying elements Zn, Cu, and Ag were relatively near to their nominal compositions (Table 2).

Besides, the EDS analysis of the alloys produced by the casting method are given in Table 3.

While producing alloys, a fixed amount of Cu (1.13 ± 0.9 wt%) and Ag were added as alloying elements according to the determined alloy (1–4 ± 0.1 wt%). It was seen that the alloy ratios planned to be produced cast within the tolerance ranges. After casting, atomic diffusion was

**Table 2**
Chemical compositions of the alloys (wt%).

| Alloys | Cu | Ag | Others | Zn |
|---|---|---|---|---|
| Pure Zn | - | - | 0.012 | bal. |
| Zn-1Cu | 1.121 | - | 0.025 | bal. |
| Zn-1Cu-1Ag | 1.185 | 1.082 | 0.034 | bal. |
| Zn-1Cu-2Ag | 1.176 | 2.132 | 0.031 | bal. |
| Zn-1Cu-3Ag | 1.143 | 3.127 | 0.035 | bal. |
| Zn-1Cu-4Ag | 1.136 | 4.158 | 0.039 | bal. |

**Table 3**
Chemical composition of pure Zn, Zn-1Cu, and Zn-1Cu-xAg alloys (wt%).

| Alloy | Zn | Cu | Ag |
|---|---|---|---|
| Pure Zn | 99.91 | - | - |
| Zn-1Cu | 98.87 | 1.13 | - |
| Zn-1Cu-1Ag | 97.98 | 1.12 | 0.90 |
| Zn-1Cu-2Ag | 97.10 | 1.02 | 1.88 |
| Zn-1Cu-3Ag | 96.20 | 1.09 | 2.90 |
| Zn-1Cu-4Ag | 95.78 | 1.12 | 4.10 |

allowed by providing sufficient time and temperature with the homogenization process conclusions.

XRD patterns of the pure Zn, Zn-1Cu, and Zn-1Cu-xAg alloys are presented in Fig. 1.

It is well known that the Ɛ-$CuZn_5$ phase solidifies first consistent with the Zn-Cu binary phase diagram. The Zn phase also forms rapidly by surrounding the Ɛ phase. Later, the peritectic transformation continues with the solid-state diffusion of Cu and Zn atoms through this Zn layer, gradually slowing down. During this process, the Ɛ-$CuZn_5$ phase goes into the solution and gives out Cu atoms by diffusion. In the layered Zn phase, the layers near the Ɛ-$CuZn_5$ phase are rich in Cu, while the Cu density decreases as the layer progresses.

In the case of equilibrium solidification, this phase is expected to dissolve completely in the Zn matrix and disperse into the structure as Cu atoms. In the case of non-equilibrium solidification, the dissolution of the primary Ɛ-$CuZn_5$ phase may be quite limited. When the temperature passes below the solvus line, the Ɛ-$CuZn_5$ phase is expected to precipitate as the secondary phase in balanced cooling. Considering the Zn-1Cu casting microstructure, it can be said that this is why the Ɛ-$CuZn_5$ phase is not seen [38,39]. In the Zn-Cu and Zn-Ag binary phase diagram, peritectic transformations are observed in the high rate of the Zn region, so peritectic transformation should also be observed in the ternary alloy. It can be said that with the addition of silver to the system, the solidification process similar to the Zn-1Cu alloy also occurs in the silver alloy casting samples.

In addition, when Fig. 1 was examined, it was also determined (Ag, Cu)$Zn_4$ phase. Considering the ternary phase diagram and starting from the literature reviews, it is logical as this is the first intermediate phase that can occur for this system [40,41]. In the Zn-1Cu-4Ag alloy, which has the highest alloy ratio, the (Ag, Cu)$Zn_4$ phase is seen as bright white. The reason why these phases reach micron sizes in the casting structure of the Zn-1Cu-4Ag alloy is that as a result of the increased alloy ratio, it precipitates as a secondary (Ag, Cu)$Zn_4$ phase instead of dispersing in the structure.

Fig. 2 shows the optical micrographs of the pure Zn, Zn-1Cu, and Zn-1Cu-xAg alloys.

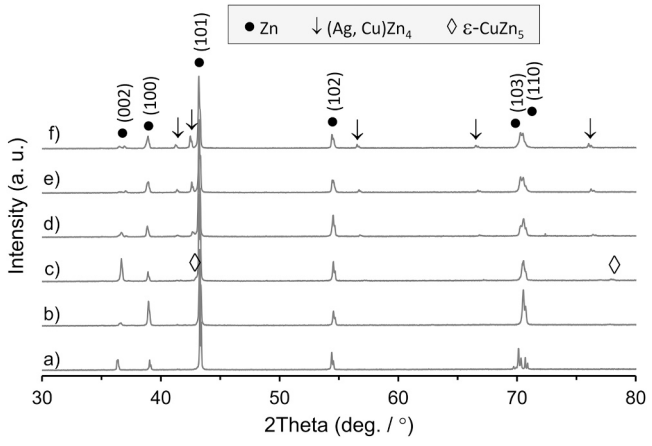


**Fig. 1.** XRD patterns of the a) pure Zn, b) Zn-1Cu, c) Zn-1Cu-1Ag, d) Zn-1Cu-2Ag, e) Zn-1Cu-3Ag, and f) Zn-1Cu-4Ag.

Pure Zn showed quite a large grain structure aligned through heat transition directions during solidification when the optical OM images were examined. The grains had twin structures in the microstructure of all samples (marked with white arrows in Fig. 2). Furthermore, the alloying increased the networks of the twins in the microstructure. The twin networks became complex after alloying with Cu and Ag. It is well known that during homogenization annealing for some as-cast alloys with dendritically cored microstructure, the diffusion mechanism produces stress fields to be trapped which could cause the existence of recrystallization or another process that might remarkably affect the twin formation [42,43]. For example, Liu et al. [42] reported that the density of twins increased with both the alloying element (Sn) content and annealing time in alloys. This is also valid for the increase of alloying elements in the present study. On the other hand, when the Zn-1Cu-4Ag alloy was examined, it was observed that the twin orientation was distributed and decreased. This may be due to the precipitates formed at the grain boundaries after annealing because the precipitates formed at the grain boundaries affect the diffusion and the twinning energy [42,44,45]. The precipitates were generally observed at grain boundaries in Zn-1Cu-3Ag samples while they were formed in-grains at Zn-1Cu-4Ag samples as shown in Fig. 2 (marked with yellow arrows). It is observed that the grain size decreases with the increase in the alloying ratio (Fig. 3). The grain size reduction drastically increases with the ratio of Ag element, which indicates that the Ag alloying element acts strongly as a grain refiner. The results are in good agreement with the findings of the refs [32,33].

### 3.2. Hardness behavior of the alloys

The average hardness values of the produced alloys comparatively with their pure Zn and Zn-1Cu counterparts are also shown in Fig. 3. The pure Zn's hardness values were measured as about 29 ( ± 2.2) HV. The alloying with 1 wt% Cu element increased the hardness of pure Zn at about 50 ( ± 1.3) HV. Similarly, the hardness progressively improved with increasing the Ag element in the Zn-1Cu master alloy. The maximum hardness value was measured as 69 ( ± 1.3) HV for Zn-1Cu-4Ag alloy, which has the highest alloy ratio among the developed alloy systems. This increase is because of the solid solution and precipitation strengthening mechanisms. Because the grain size reduction by the heterogeneous nucleation and grain boundary hardening (Hall Patch relation) increases the hardness and strength of the alloys [11,46]. It is noticeable that the strengthening effect of Cu and Ag at the maximum solubility becomes much stronger because of their relatively high solubility in the Zn matrix. This is also due to Ag and Cu atomic radii (0.144 nm and 0.128 nm, respectively) being so close to those of Zn (0.134 nm) [47,48].

There is no difference crystallographically, between the annealing and deformation twins [49]. Besides, the twins can strongly inhibit dislocation slippage by acting as grain boundaries in the structure, which may cause the alloy to harden [50–52]. Therefore, the hardness values of the alloys were evaluated with Figs. 1 and 3 outputs together, the hardness increase is rising due to the (Ag, Cu)$Zn_4$ phase starting to appear as seen in XRD patterns (Fig. 1) after 1 wt% Ag adding to Zn-1Cu master alloy. The results confirm that the hardness values increase in parallel with the increase in the alloying element ratio with the effect of the hard phases formed in the structure of Zn-1Cu-3Ag and Zn-1Cu-4Ag by the alloying (Fig. 2).

### 3.3. Evaluation of in-vitro corrosion and immersion tests

The potentiodynamic scanning (PDS) curves of alloys under in-vitro conditions (in AU electrolyte at body temp.) are presented in Fig. 4. Besides, important electrochemical corrosion parameters calculated from these curves are also given in Table 4. These parameters are corrosion current density ($I_{corr}$), corrosion potential ($E_{corr}$), corrosion rate ($CR$), and polarization resistance ($R_p$).

The $E_{ocp}$ values of the produced alloys were monitored in the AU electrolyte at body temperature for at least 40 min. The $E_{ocp}$ values of

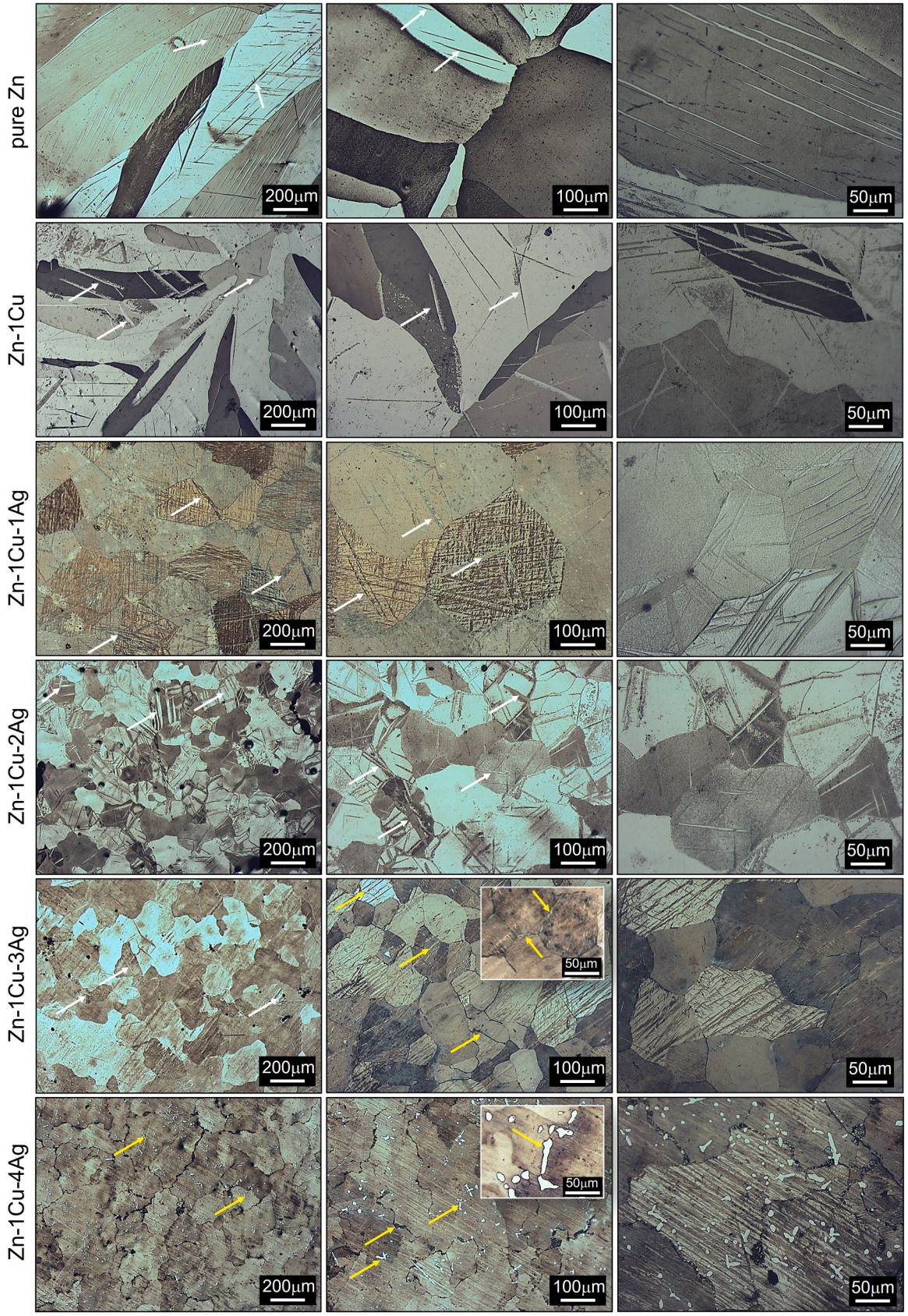


**Fig. 2.** Optical microscope images of the pure Zn, Zn-1Cu, and Zn-1Cu-xAg alloys (white arrows show twins, and yellow arrows show precipitations on the images).

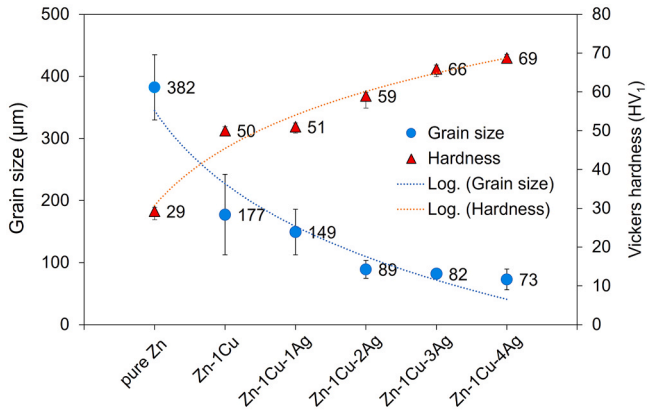


**Fig. 3.** Average grain sizes of the pure Zn, Zn-1Cu, and Zn-1Cu-xAg alloys.

the alloys reached stable values, demonstrating the following: − 1160 mV for pure-Zn, − 940 mV for Zn-1Cu, − 975 mV for Zn-1Cu-1Ag, − 1070 mV for Zn-1Cu-2Ag, − 1075 mV for Zn-1Cu-3Ag, − 1050 mV for Zn-1Cu-4Ag. By the way, the $E_{corr}$ values presented in this study were within the ranges reported in the literature in different simulated body fluids [2].

The highest and lowest $I_{corr}$ values were calculated in Zn-1Cu and Zn-1Cu-3Ag alloys as 17.13 and 1.318 mA·cm$^{-2}$, respectively. Besides, the polarization resistance of the alloys increased with increasing the Ag ratio in the Zn-1Cu master alloy. This is probably due to the grain refinement in the Zn-1Cu alloys to the addition of Ag. Some researchers have reported the general opinion that the refinement in grain size of Zn and Mg-based biodegradable alloys provides better corrosion resistance in NaCl electrolytes [53–56]. However, the corrosion resistance again decreased rapidly with the 4 wt% Ag additions to Zn-1Cu. The larger the cathodic areas (nobler intermetallic $CuZn_5$ phases, and Cu-rich regions) in Zn-1Cu alloy compared with pure Zn forms, the bigger the galvanic current in the alloy (Table 4). The rapid decrease in the cathodic branches of the PDS curves indicates an activation-controlled corrosion mechanism in the alloys.

The $E_{corr}$ value of the pure Zn was towards the move to nobler values with the addition of Cu due to the big difference between the standard electrode potentials of Zn (−0.76 V) and Cu (−0.34 V). The big potential difference triggers the formation of micro-galvanic cells between Zn-Cu grains and $CuZn_4$/$CuZn_5$ phases in the microstructure and causes heavy corrosion damage in the structure [57]. Thus, a sudden increase was observed in the corrosion rate after the Cu-addition (0.256 mpy) to the pure-Zn (0.054 mpy). Notably, the degradation rate of the Zn-1Cu alloy

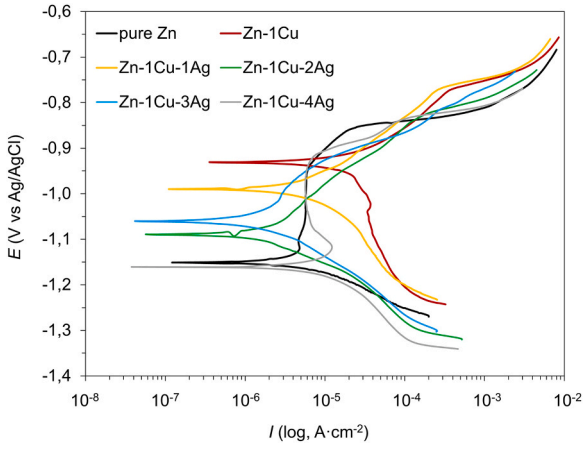


**Fig. 4.** The comparison of the PDS curves of pure Zn, Zn-1Cu, and Zn-1Cu-xAg alloys under in-vitro conditions.

**Table 4**
Electrochemical corrosion parameters of the alloys calculated from the PDS curves.

| Alloy | $E_{corr}$ (mV) | $I_{corr}$ (μA·cm$^{-2}$) | $R_p$ (ohm·cm$^{-2}$) | *CR* (mpy) |
|---|---|---|---|---|
| Pure Zn | -1151 | 3.581 | 4761 | 0.054 |
| Zn-1Cu | -930 | 17.130 | 1763 | 0.256 |
| Zn-1Cu-1Ag | -991 | 6.912 | 4596 | 0.105 |
| Zn-1Cu-2Ag | -1093 | 2.302 | 11648 | 0.036 |
| Zn-1Cu-3Ag | -1060 | 1.318 | 17185 | 0.021 |
| Zn-1Cu-4Ag | -1161 | 9.480 | 2448 | 0.152 |

was higher than about four times that of pure-Zn. In the morphological analyses of the pure-Zn and Zn-1Cu alloys after the corrosion test, heavy corrosion marks were visible on the Zn-1Cu surface, relatively (Fig. 5).

However, after the Ag ratio (>2 wt%) in the master alloy reached a dominant rate, the $E_{corr}$ value of the alloys again approached the $E_{corr}$ value of pure Zn. By the way, according to Table 4 and Fig. 4, there were slight differences in $E_{ocp}$ and $E_{corr}$ values of the alloys probably due to the corrosion products formed at electrolyte/film interfaces [57]. Besides, a clear breakdown was observed in the passivation region (plateau region) of pure-Zn and Zn-1Cu-4Ag alloy during the anodic scanning (Fig. 4). In other words, pitting corrosion more dominantly occurred in the samples. The reduction of grain size and presence of small intermetallic phases ($AgZn_4$) after the addition of 4 wt% Ag contributed to many pit formations on the alloy surfaces and caused more uniform corrosion marks in the samples (Fig. 5a and Fig. 6d) [46]. By the way, it is noteworthy that the number of corrosion nucleation points increases with the increasing amount of Ag in the Zn-1Cu master alloy (Fig. 6). However, the size of the pits is smaller with increasing the Ag. The observations also agreed with PDS results (Fig. 4 and Table 4).

Fig. 7 shows corrosion products (oxides and hydroxides) accumulated on the film of the Zn-1Cu-1Ag alloy.

It is well known that different factors that affect the corrosion behaviors of metallic alloys such as chemical composition, grain size, or presence of intermetallic phases [8,29–31,58–60]. However, probably the main factor, causing the cracking of the protective surface film and the progression of corrosion on the surface, is the thermal expansion differences between the alloy and formed oxide film on its surface. Besides, the locally mixed potential differences of the oxide film due to the presence of intermetallic phases in it, and alloy composition increases this effect. Undoubtedly, aggressive $Cl^-$ ions in the AU electrolyte especially attack these cracks in the film (such as region 1 in Fig. 7), where the pit progress in depth or as filiform and increases the corrosion failure on the surface (region 2 in Fig. 7). Finally, increasing the polarization level increased the corrosion products such as $Zn(OH)_2$ or ZnO, significantly (Fig. 7b) according to following equations: $2Zn^{2+} + 4OH^- \rightarrow 2Zn(OH)_2$ and $Zn(OH)_2 \rightarrow ZnO + H_2O$ [30,61]. In addition, it has been reported that $ZnCl_2$ salts can be formed in corroded films as a result of the reaction of $Cl^-$ ions in the electrolyte with these oxides [35,46]. When all experimental results are evaluated together, it was seen that the Zn-1Cu-1Ag and Zn-1Cu-4Ag samples have a high degradation rate among the Ag alloyed samples.

Immersion tests are also an essential evaluation method for biodegradable metallic implant materials. Besides, the immersion tests use to evaluate the biodegradation trend of the material and to determine how it will perform over time in the body [62]. The tests involve immersing the implant material in the simulated environments for a specified period. Overall, immersion tests play a crucial role in the progression and evaluation of biodegradable metallic implant materials. Thus, samples were submerged in the AU electrolyte for 1, 7, 14, and 21 days at body temperature (37 °C) in this study, and the samples were evaluated for changes in weight loss and their biodegradation rate during the immersion period.

The weight loss of each sample was calculated to the following eq. [63]: $W_t\% = 100 \times \frac{(W_f - W_i)}{W_i}$, where $W_i$ is the initial dry weight of the alloy

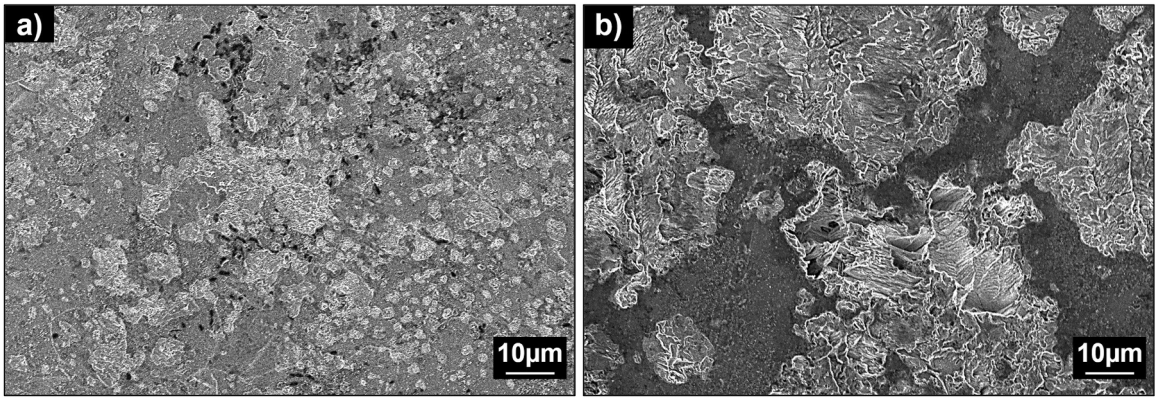


**Fig. 5.** SEM images of corroded surfaces of a) pure-Zn, and b) Zn-1Cu alloy.

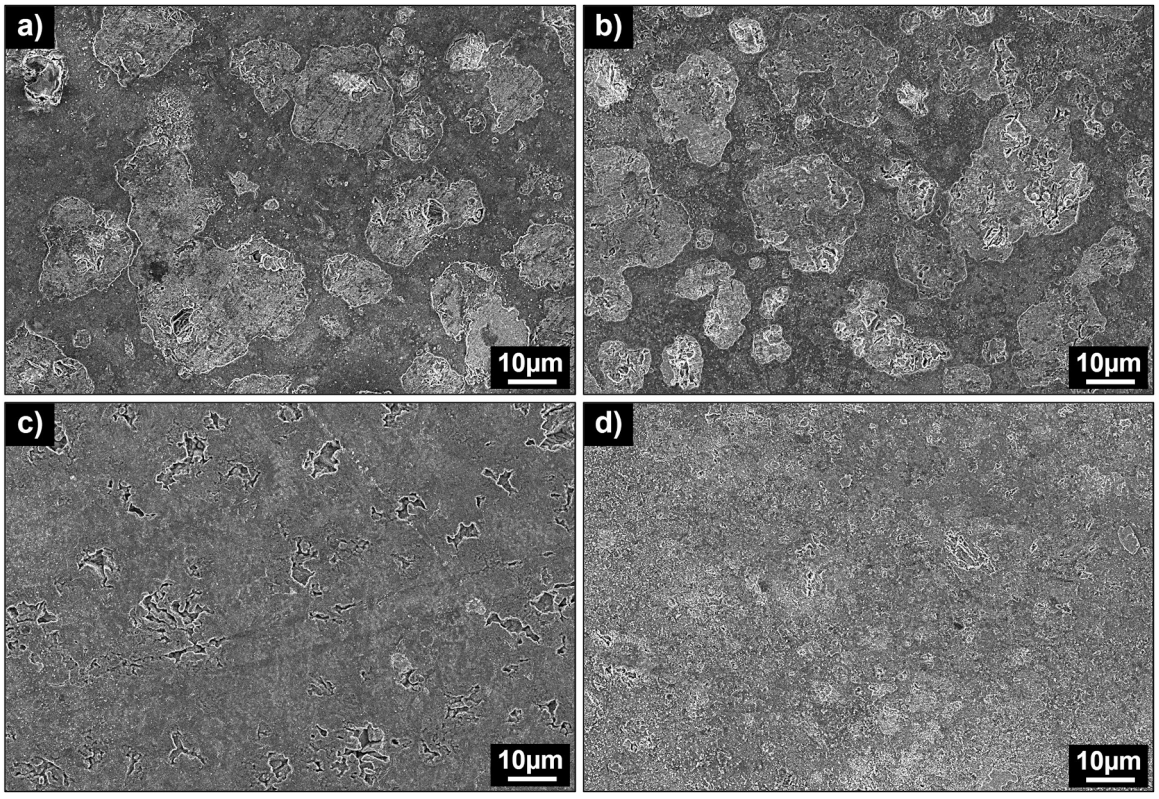


**Fig. 6.** SEM images of the corroded surfaces of a) Zn-1Cu-1Ag, b) Zn-1Cu-2Ag, c) Zn-1Cu-3Ag, and d) Zn-1Cu-4Ag alloys under in-vitro conditions.

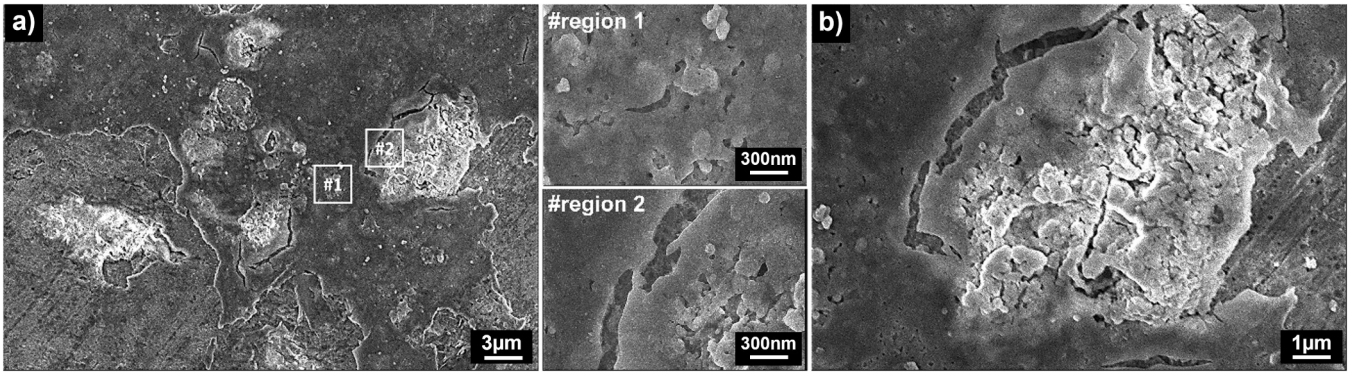


**Fig. 7.** The corrosion morphology of the Zn-1Cu-1Ag alloy at the extensive stage of polarization: a) lower and b) higher magnifications.

and $W_f$ is the dry weight of the alloy after immersion test. The corrosion rate was determined with the $CR = \frac{K \bullet W_t}{A \bullet t \bullet \rho}$ formula described in ref. [57], where $CR$ means to the corr. rate, $W_t$ the weight loss of the alloy as described above, $A$ the corroded area, ρ is the density, and $t$ is immersion time.

Fig. 8 shows the weight loss in AU at 37 °C, and calculated degradation rates of produced alloys. In the 21-day test results, it was determined that the Zn-1Cu-1Ag alloy had the highest degradation rate and this value was 0.135 mm·year$^{-1}$. This result was relatively in well-agreement with the electrochemical results presented above (Table 4). The other samples had a near degradation rate each other at the end of the 21st day which indicates the reliability of the electrochemical tests.

The comparative analysis of the immersion and electrochemical corrosion tests provides valuable insights into the corrosion behavior of Zn-Cu-Ag alloys. In the electrochemical corrosion tests, the Zn-1Cu-3Ag alloy demonstrated the lowest corrosion rate with 0.021 mpy, indicating its lower degradation rate in all samples. But it was noted that the Zn-1Cu-2Ag alloy (0.036 mpy) exhibited a corrosion rate that was remarkably close to that of Zn-1Cu-3Ag, suggesting its potential as a similar behavior to corrosion. Both alloys displayed high polarization resistances, indicating their ability to withstand aggressive AU electrolytes. In contrast, the Zn-1Cu-1Ag and Zn-1Cu-4Ag alloys exhibited corrosion rates that were over four times higher than Zn-1Cu-2Ag and Zn-1Cu-3Ag, highlighting their higher degradation rate. At the end of the 1 day of the immersion tests, all the Zn-Cu-Ag alloys demonstrated significantly higher degradation rates (average 1.26 mm•year-1) compared to pure Zn sample (~0.7 mm•year-1), indicating their increased susceptibility to degradation in the AU environment. However, after 7 days, the degradation rates of the alloys decreased dramatically, suggesting the formation of a protective passive layer, probably (Fig. 8). Among the alloys, the Zn-1Cu-2Ag alloy exhibited the lowest degradation rate (0.01543 mm•year-1) after 21 days, indicating its higher corrosion resistance in the AU solution. In contrast, the Zn-1Cu-1Ag alloy showed the highest degradation rate among all the samples at 0.1797 mm•year-1. The degradation rates of the other alloys were relatively close to each other (~0.033 mm•year-1). These findings emphasize the influence of alloy composition on the corrosion behavior of Zn-Cu-Ag alloys. The addition of Cu and Ag elements in specific ratios can significantly affect the corrosion rate, with Zn-1Cu-2Ag and Zn-1Cu-3Ag alloys demonstrating higher performance in the AU environments.

### 3.4. Bacterial sensitivity of the alloys

The antibacterial activity against *E. coli* and *S. aureus* were studied in pure Zn, Zn-1Cu, and Zn-1Cu-xAg alloys groups as shown in Fig. 9.

The bacteria were incubated in a growth medium with the uncoated and these material groups. The inhibition rate of the Zn-1Cu-1Ag was higher than the inhibition rates of the other groups on *E. coli* and *S. aureus*. When the average of inhibition rate was 18.5 mm in Zn-1Cu-1Ag, 11.5 mm in pure Zn, 14.1 mm in Zn-1Cu, 15.3 mm in Zn-1Cu-2Ag, 14.5 mm in Zn-1Cu-3Ag, 17.3 mm in Zn-1Cu-4Ag in the *E. coli* incubation (Fig. 9a). Similarly, average of inhibition rate was 16.5 mm in Zn-1Cu-1Ag, 12.5 mm in the pure Zn, 13.5 mm in Zn-1Cu, 14.5 mm in Zn-1Cu-2Ag, 15.1 mm in Zn-1Cu-3Ag, 16 mm in Zn-1Cu-4Ag in the *S. aureus* incubation (Fig. 9b). Ag can directly react with the membrane of the bacteria, because of the large membrane area, resulting in more efficient interaction. Silver ions bind negatively charged proteins and nucleic acids, causing structural changes and deformations in the bacterial cell's walls, membranes, and nucleic acids. Ag is most likely to affect the respiratory chain in bacterial cells [64,65]. As a result, combinations of Zn-1Cu and Ag blocked bacteria and demonstrated a strong antibacterial property.

### 3.5. Cell survival/death in prostate epithelial and bladder cancer cells of the alloys

Fluorescence images of the PNT1A prostate epithelial cells were taken on the pure Zn, Zn-1Cu, and Zn-1Cu-xAg alloys, respectively (Fig. 10). Besides, seeded cells onto the empty cell culture dishes to evaluate the cell structure before seeding them onto different samples. DiOC6 staining indicates a healthy cell population with active mitochondria and inner membrane network, the cells were stained on the pure Zn, Zn-1Cu, and Zn-1Cu-3Ag alloys on the materials. Other samples did not show cell attachment to the material (Fig. 11). However, the shape of the cells on the attached zones did not show similarity to untreated control. While untreated cells were alive and not showing

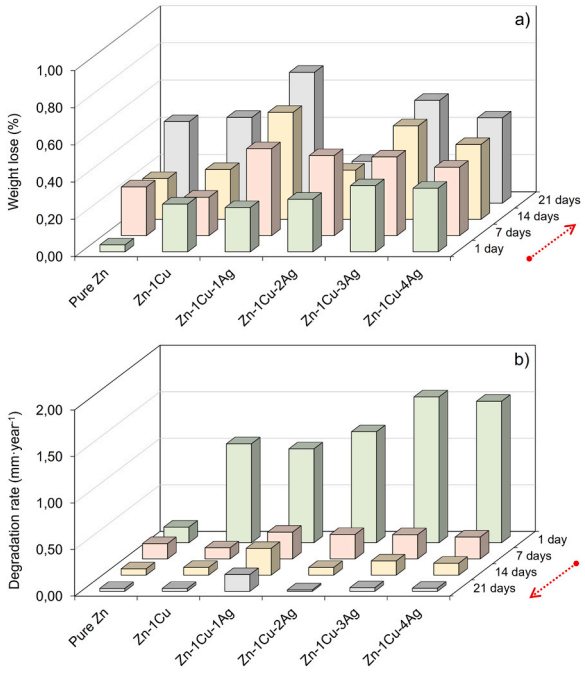


**Fig. 8.** a) Weight lost values, and b) degradation rates of pure Zn, Zn-1Cu, and Zn-1Cu-xAg alloys measured by immersion tests in AU solution at 37°C.

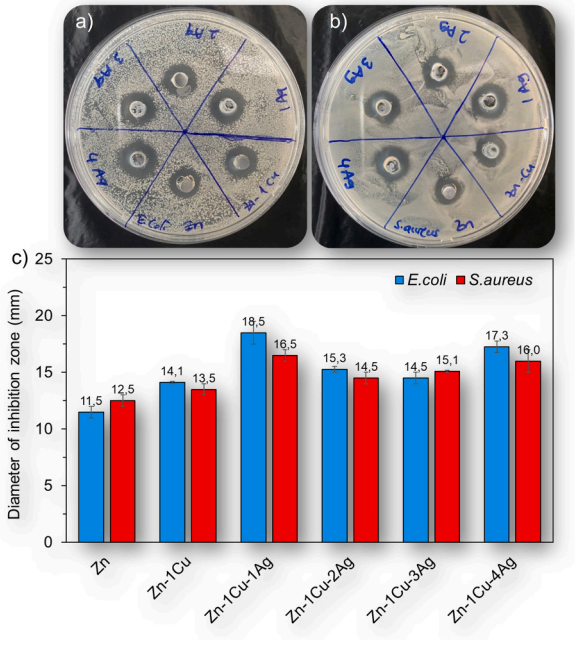


**Fig. 9.** Antibacterial effects of the pure Zn, Zn-1Cu, and Zn-1Cu-xAg alloys at 24 h against a) *E. coli*, b) *S. aureus*, and c) histogram of inhibition zone diameters obtained after antibiotic susceptibility test with against *E. coli* and *S. aureus* incubation.

propidium iodide (PI) staining on a petri dish, pure Zn, Zn-1Cu, and Zn-1Cu-3Ag led to an increased dead cell population within 48 h (Fig. 11). In accordance with previous findings [8–11], metal alloys are promising to increase cell viability on the material or at the edge of the produced samples. Similarly, both cell lines showed different sensitivities against a mixture of zinc, silver, and copper metals. Optimization of the mixtures increased the biocompatibility of the produced materials.

In addition, it was checked the healthy/dead status of the cells via fluorescence microscopy on the side of the samples (Fig. 12). The fluorescence images of T24 human urinary bladder cancer cells for the Zn (pure), Zn-1Cu, Zn-1Cu-1Ag, Zn-1Cu-2Ag, Zn-1Cu-3Ag, Zn-1Cu-4Ag were taken with a fluorescent microscope. Before seeding cells on the samples, the cells were seeded onto the plate as a control, and the cellular morphology was observed (Fig. 13).

Zn-1Cu-2Ag was the most promising material compared to others due to the increased number of viable cells stained with DiOC6. Concomitantly, PI-stained cells were also detectable on the Zn-1Cu-2Ag compared to pure Zn, Zn-1Cu, and Zn-1Cu-3Ag. Zn-1Cu-3Ag showed a diminished number of attached T24 cells on material with less PI staining for the dead cell population. However, we did not obtain any staining results for cells on the Zn-1Cu-1Ag and Zn-1Cu-4Ag (data not shown). The cell morphology was not the same with untreated control T24 cells (Fig. 13). The cells attached to the Petri dishes near the material were promising for T24 cells (Fig. 14). All samples except Zn-1Cu showed promising results for the number of attached cells near the material within 48 h. The best results like pure Zn were obtained from Zn-1Cu-1Ag, Zn-1Cu-2Ag, and Zn-1Cu-3Ag with higher cytoplasmic content compared to Zn-1Cu and Zn-1Cu-4Ag. The increasing amount of Ag in the alloys caused a significant decrease in the attached cell number on the material or side.

In this study, the Zn-Cu-Ag alloys have been studied for urological applications such as ureteral stents. All results have been considered together, Zn-1Cu-1Ag alloy exhibited promising behaviors such as adequate biodegradation rate and cellular responses for the primary cells. Consequently, these materials have the potential to provide a more natural healing process and reduce the risk of implant-related complications. However, only static degradation behavior was investigated in this paper, further research is needed to fully evaluate the performance and in-vitro dynamic degradation tests simulated by a human ureter channel, biomechanical and in-vivo studies.

## 4. Conclusions

In this study, the biodegradable Zn-Cu-xAg (x: 1, 2, 3, and 4) alloys have been fabricated by a low-cost casting method, successfully. It has been revealed that the grains get smaller with the increase of the Ag element ratio. Thus, it can be concluded that Ag acts as a grain refiner for this ternary system. By the way, the (Ag, Cu)$Zn_4$ phase has been precipitated as a secondary phase during the heat treatment. However, the dissolution of the primary Ɛ-$CuZn_5$ phase was quite limited in the lower content of Ag in the Zn matrix. The hardness values of the Zn-1Cu master alloy were gradually increased with the increasing Ag content as expected. The maximum hardness was measured as 69 ( $\pm$ 1.3) HV for Zn-1Cu-4Ag alloy, which has the highest alloy ratio among the developed alloy systems, due to the solid solution strengthening and precipitation hardening. The highest and lowest $I_{corr}$ values, which are references also corrosion rate, were calculated in Zn-1Cu and Zn-1Cu-3Ag alloys as 17.13 and 1.318 mA·$cm^{-2}$, respectively. The big potential differences between the alloying elements and precipitates trigger the formation of micro-galvanic cells in Zn-Cu-xAg alloy and cause heavy corrosion damage in the microstructure. The morphological observations after the corrosion tests in the AU electrolyte showed that the number of corrosion nucleation points increases with the increasing amount of Ag in the Zn-1Cu master alloy. However, the size of the pits is smaller with increasing Ag. Besides, the results of the bacterial test revealed that Zn-1Cu and 1Ag combinations had a better antibacterial impact than other combinations. However, the increasing amount of Ag in the samples caused a significant decrease in the attached cell number on the material or by the side for both PNT1A prostate epithelial or T24 urothelial carcinoma cells. Although PNT1A cells responded better against Zn-1Cu, T24 cells did not adhere to or side of the material. For both cell lines, Zn-1Cu-1Ag was the most promising material for the number of attached cells. Considering both the hardness, corrosion, and cell culture tests together, the Zn-1Cu-3Ag system is the best option for the stent to withstand the high radial forces exerted by the vessel without shrinking under in-vitro conditions.

### CRediT authorship contribution statement

H. Yilmazer: Resources, Investigation, Project administration, Validation, Writing – original draft. S. Basit: Investigation, Writing – original

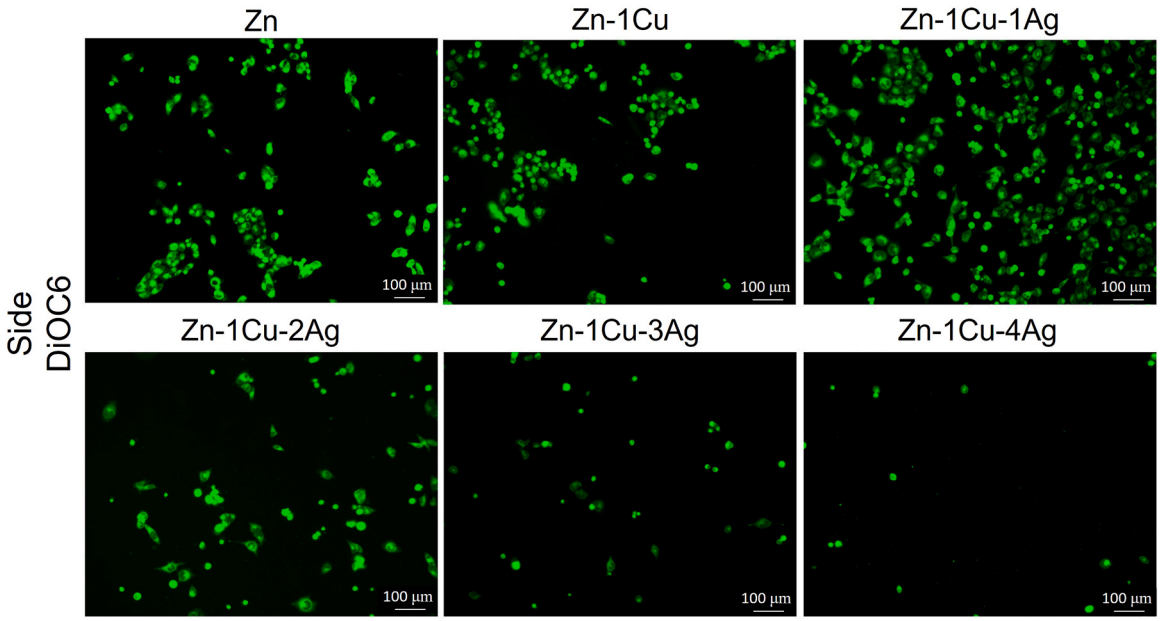


**Fig. 10.** Fluorescence images of PNT1A prostate epithelial cells were taken following DiOC6 staining at the side of the materials at 48 h.

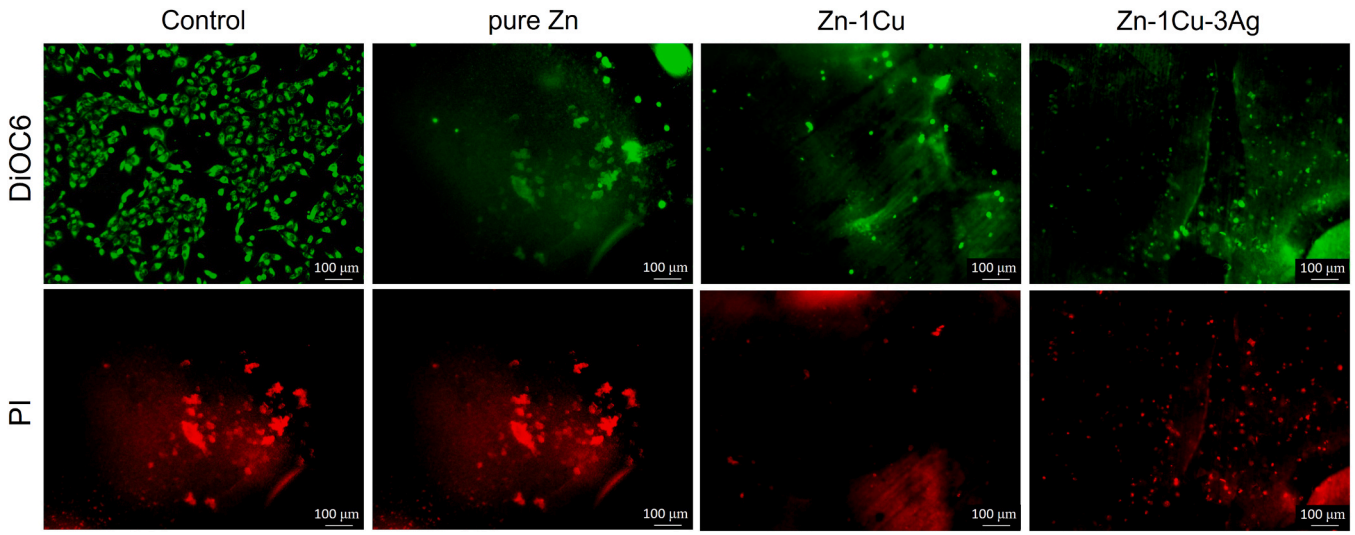


**Fig. 11.** Fluorescence images of PNT1A prostate epithelial cells were taken following DiOC6 staining (up), and PI staining (down) on the materials at 48 h.

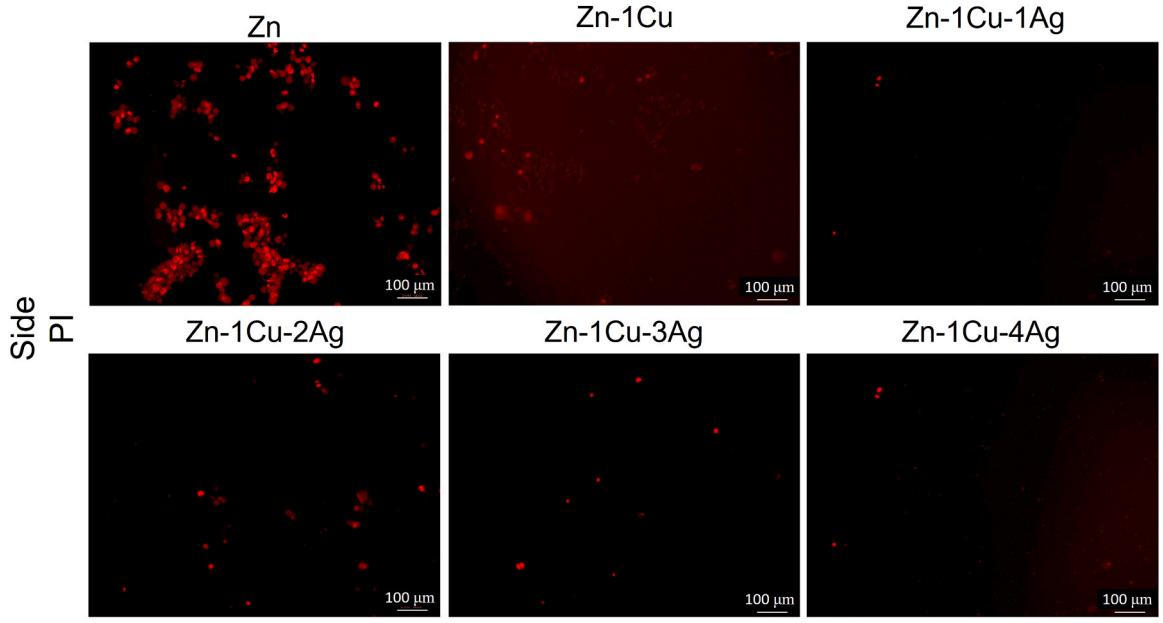


**Fig. 12.** Fluorescence images of PNT1A prostate epithelial cells were taken following PI staining at the side of the samples at 48 h.

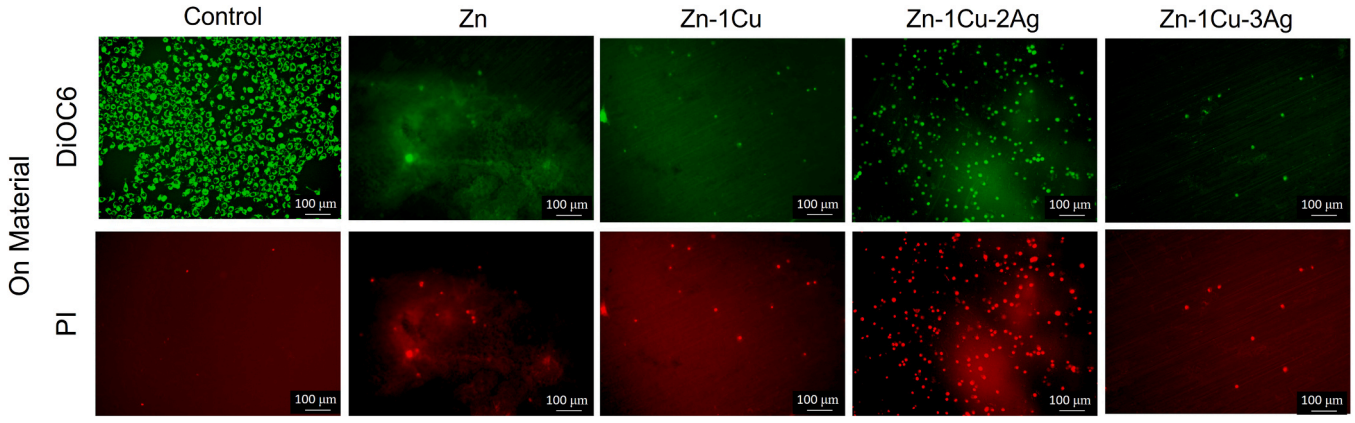


**Fig. 13.** Fluorescence images of T24 human urinary bladder cancer cells were taken following DiOC6 staining (green) and PI staining (red) on the materials at 48 h.

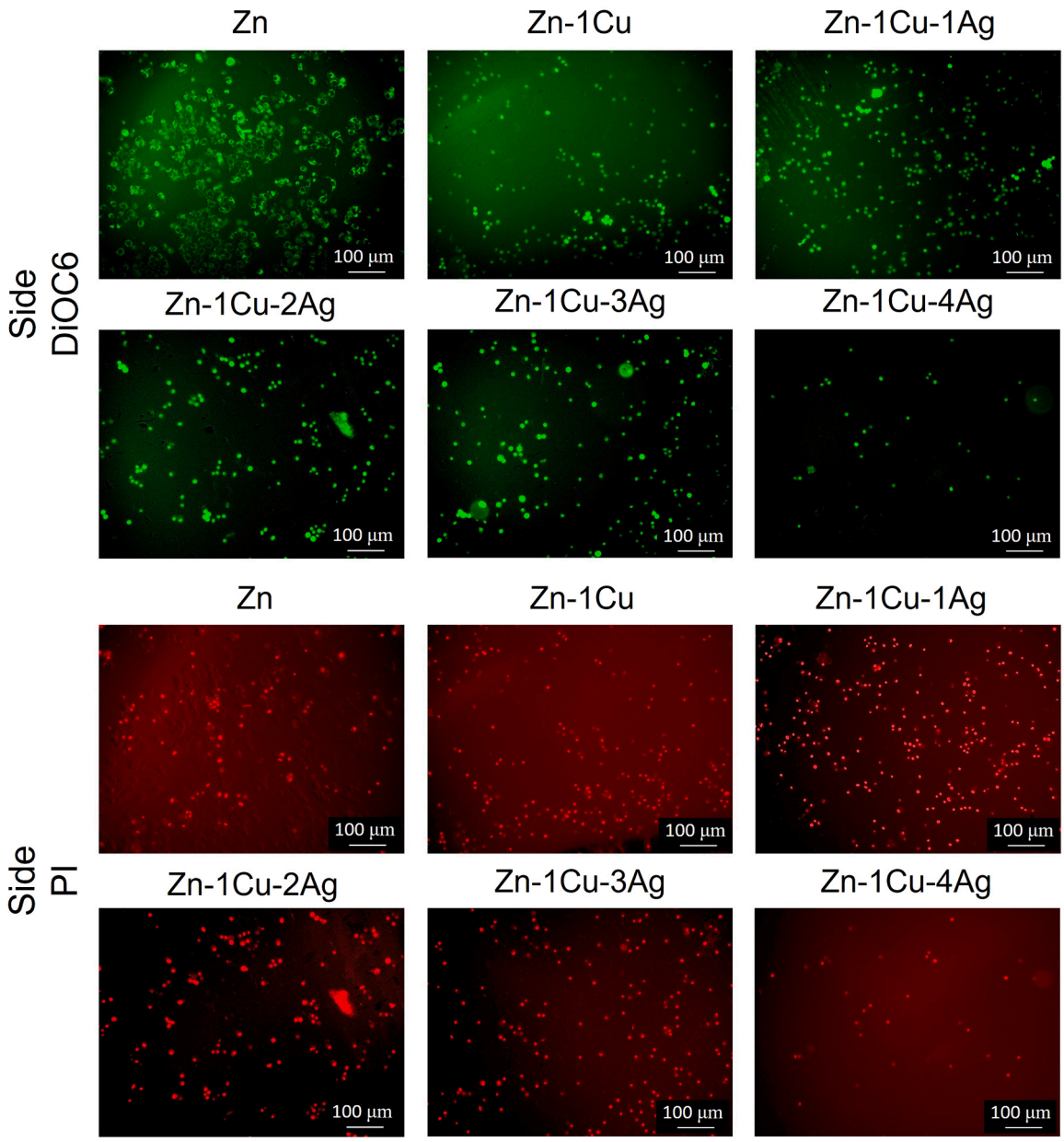


**Fig. 14.** Fluorescence images of T24 human urinary bladder cancer cells were taken following DiOC6 staining (green) and PI staining (red) at the side of the samples at 48 h.

draft. A. Sen: Formal Analysis, Methodology, Validation. Y. Yilmazer: Methodology, Validation, Writing – original draft. B. Dalbayrak: Formal Analysis, Methodology, Validation. E. D. Arisan: Methodology, Validation, Writing – original draft. S. Arisan: Methodology, Validation. R. K. Islamgaliev: Resources, Investigation, Project administration. Burak Dikici: Conceptualization, Supervision, Methodology, Validation, Writing – original draft, Visualization.

## Declaration of Competing Interest

The authors declare that they have no known competing financial interests or personal relationships that could have appeared to influence the work reported in this paper.

## Data availability

Data will be made available on request.

## Acknowledgment

The authors are highly thankful to the Scientific and Technological Research Council of Turkey (TUBITAK, grant number: 220N139) and the Russian Foundation for Basic Research (RFBR, grant number: 21-53-46017) for financial support.

## References

[1] S. Amukarimi, M. Mozafari, Biodegradable magnesium-based biomaterials: An overview of challenges and opportunities, MedComm 2 (2021) 123–144, https://doi.org/10.1002/mco2.59.

[2] D. Hernández-Escobar, S. Champagne, H. Yilmazer, B. Dikici, C.J. Boehlert, H. Hermawan, Current status and perspectives of zinc-based absorbable alloys for biomedical applications, Acta Biomater. 97 (2019) 1–22, https://doi.org/10.1016/j.actbio.2019.07.034.

[3] H.-S. Han, S. Loffredo, I. Jun, J. Edwards, Y.-C. Kim, H.-K. Seok, F. Witte, D. Mantovani, S. Glyn-Jones, Current status and outlook on the clinical translation of biodegradable metals, Mater. Today 23 (2019) 57–71, https://doi.org/10.1016/j.mattod.2018.05.018.

[4] H. Hermawan, Updates on the research and development of absorbable metals for biomedical applications, Prog. Biomater. 7 (2018) 93–110, https://doi.org/10.1007/s40204-018-0091-4.

[5] W. Ding, Opportunities and challenges for the biodegradable magnesium alloys as next-generation biomaterials, Regen. Biomater. 3 (2016) 79–86, https://doi.org/10.1093/rb/rbw003.

[6] Q. Tian, C. Zhang, M. Deo, L. Rivera-Castaneda, N. Masoudipour, R. Guan, H. Liu, Responses of human urothelial cells to magnesium-zinc-strontium alloys and associated insoluble degradation products for urological stent applications, Mater. Sci. Eng. C. 96 (2019) 248–262, https://doi.org/10.1016/j.msec.2018.11.018.

[7] L. Wang, G. Yang, H. Xie, F. Chen, Prospects for the research and application of biodegradable ureteral stents: from bench to bedside, J. Biomater. Sci. Polym. 29 (2018) 1657–1666, https://doi.org/10.1080/09205063.2018.1498184.

[8] Y.F. Zheng, X.N. Gu, F. Witte, Biodegradable metals, Mater. Sci. Eng. R. Rep. 77 (2014) 1–34, https://doi.org/10.1016/j.mser.2014.01.001.

[9] Y.B. Wang, H.F. Li, Y.F. Zheng, M. Li, Corrosion performances in simulated body fluids and cytotoxicity evaluation of Fe-based bulk metallic glasses, Mater. Sci. Eng. C. 32 (2012) 599–606, https://doi.org/10.1016/j.msec.2011.12.018.

[10] S. Agarwal, J. Curtin, B. Duffy, S. Jaiswal, Biodegradable magnesium alloys for orthopaedic applications: A review on corrosion, biocompatibility and surface modifications, Mater. Sci. Eng. C. 68 (2016) 948–963, https://doi.org/10.1016/j.msec.2016.06.020.

[11] J.-M. Seitz, M. Durisin, J. Goldman, J.W. Drelich, Recent advances in biodegradable metals for medical sutures: a critical review, Adv. Healthc. Mater. 4 (2015) 1915–1936, https://doi.org/10.1002/adhm.201500189.

[12] C.L. Lu, H.Y. Dong, W. Wang, G. Yang, In Vivo and in Vitro Studies of Biodegradable WE43 Stent, in: Appl. Mech. Mater., Trans Tech Publications Ltd, 2014, pp. 70–76, https://doi.org/10.4028/www.scientific.net/amm.528.70.

[13] P. Peeters, M. Bosiers, J. Verbist, K. Deloose, B. Heublein, Preliminary results after application of absorbable metal stents in patients with critical limb ischemia, J. Endovasc. Ther. 12 (2005) 1–5, https://doi.org/10.1583/04-1349R.1.

[14] J. Kuhlmann, I. Bartsch, E. Willbold, S. Schuchardt, O. Holz, N. Hort, D. Höche, W. R. Heineman, F. Witte, Fast escape of hydrogen from gas cavities around corroding magnesium implants, Acta Biomater. 9 (2013) 8714–8721, https://doi.org/10.1016/j.actbio.2012.10.008.

[15] M. Schinhammer, A.C. Hänzi, J.F. Löffler, P.J. Uggowitzer, Design strategy for biodegradable Fe-based alloys for medical applications, Acta Biomater. 6 (2010) 1705–1713, https://doi.org/10.1016/j.actbio.2009.07.039.

[16] A. Drynda, T. Hassel, F.W. Bach, M. Peuster, In vitro and in vivo corrosion properties of new iron-manganese alloys designed for cardiovascular applications, J. Biomed. Mater. Res. Part B Appl. Biomater. 103 (2015) 649–660, https://doi.org/10.1002/jbm.b.33234.

[17] M. Wątroba, W. Bednarczyk, J. Kawałko, K. Mech, M. Marciszko, G. Boelter, M. Banzhaf, P. Bała, Design of novel Zn-Ag-Zr alloy with enhanced strength as a potential biodegradable implant material, Mater. Des. 183 (2019), https://doi.org/10.1016/j.matdes.2019.108154.

[18] M.S. Dambatta, S. Izman, D. Kurniawan, S. Farahany, B. Yahaya, H. Hermawan, Influence of thermal treatment on microstructure, mechanical and degradation properties of Zn-3Mg alloy as potential biodegradable implant material, Mater. Des. 85 (2015) 431–437, https://doi.org/10.1016/j.matdes.2015.06.181.

[19] H.F. Li, X.H. Xie, Y.F. Zheng, Y. Cong, F.Y. Zhou, K.J. Qiu, X. Wang, S.H. Chen, L. Huang, L. Tian, L. Qin, Development of biodegradable Zn-1X binary alloys with nutrient alloying elements Mg, Ca and Sr, Sci. Rep. 5 (2015), https://doi.org/10.1038/srep10719.

[20] H. Gong, K. Wang, R. Strich, J.G. Zhou, In vitro biodegradation behavior, mechanical properties, and cytotoxicity of biodegradable Zn-Mg alloy, J. Biomed. Mater. Res. Part B Appl. Biomater. 103 (2015) 1632–1640, https://doi.org/10.1002/jbm.b.33341.

[21] C. Wang, Z. Yu, Y. Cui, Y. Zhang, S. Yu, G. Qu, H. Gong, Processing of a novel Zn alloy micro-tube for biodegradable vascular stent application, J. Mater. Sci. Technol. 32 (2016) 925–929, https://doi.org/10.1016/j.jmst.2016.08.008.

[22] H. Li, H. Yang, Y. Zheng, F. Zhou, K. Qiu, X. Wang, Design and characterizations of novel biodegradable ternary Zn-based alloys with IIA nutrient alloying elements Mg, Ca and Sr, Mater. Des. 83 (2015) 95–102, https://doi.org/10.1016/j.matdes.2015.05.089.

[23] X. Liu, J. Sun, Y. Yang, F. Zhou, Z. Pu, L. Li, Y. Zheng, Microstructure, mechanical properties, in vitro degradation behavior and hemocompatibility of novel Zn-Mg-Sr alloys as biodegradable metals, Mater. Lett. 162 (2016) 242–245, https://doi.org/10.1016/j.matlet.2015.07.151.

[24] X. Liu, J. Sun, F. Zhou, Y. Yang, R. Chang, K. Qiu, Z. Pu, L. Li, Y. Zheng, Micro-alloying with Mn in Zn-Mg alloy for future biodegradable metals application, Mater. Des. 94 (2016) 95–104, https://doi.org/10.1016/j.matdes.2015.12.128.

[25] R. Yue, H. Huang, G. Ke, H. Zhang, J. Pei, G. Xue, G. Yuan, Microstructure, mechanical properties and in vitro degradation behavior of novel Zn-Cu-Fe alloys, Mater. Charact. 134 (2017) 114–122, https://doi.org/10.1016/j.matchar.2017.10.015.

[26] G. Gąsior, J. Szczepański, A. Radtke, Biodegradable iron-based materials—what was done and what more can be done? Materials 14 (2021) 3381, https://doi.org/10.3390/ma14123381.

[27] Y.Q. Guo, S.H. Zhang, I.J. Beyerlein, D. Legut, S.L. Shang, Z.K. Liu, R.F. Zhang, Synergetic effects of solute and strain in biocompatible Zn-based and Mg-based alloys, Acta Mater. 181 (2019) 423–438, https://doi.org/10.1016/j.actamat.2019.09.059.

[28] J. Niu, Z. Tang, H. Huang, J. Pei, H. Zhang, G. Yuan, W. Ding, Research on a Zn-Cu alloy as a biodegradable material for potential vascular stents application, Mater. Sci. Eng. C. 69 (2016) 407–413, https://doi.org/10.1016/j.msec.2016.06.082.

[29] Z. Tang, J. Niu, H. Huang, H. Zhang, J. Pei, J. Ou, G. Yuan, Potential biodegradable Zn-Cu binary alloys developed for cardiovascular implant applications, J. Mech. Behav. Biomed. Mater. 72 (2017) 182–191, https://doi.org/10.1016/j.jmbbm.2017.05.013.

[30] M. Sikora-Jasinska, E. Mostaed, A. Mostaed, R. Beanland, D. Mantovani, M. Vedani, Fabrication, mechanical properties and in vitro degradation behavior of newly developed Zn[sbnd]Ag alloys for degradable implant applications, Mater. Sci. Eng. C. 77 (2017) 1170–1181, https://doi.org/10.1016/j.msec.2017.04.023.

[31] C. Chen, R. Yue, J. Zhang, H. Huang, J. Niu, G. Yuan, Biodegradable Zn-1.5Cu-1.5Ag alloy with anti-aging ability and strain hardening behavior for cardiovascular stents, Mater. Sci. Eng. C. 116 (2020), 111172, https://doi.org/10.1016/j.msec.2020.111172.

[32] T. Di, Y. Xu, D. Liu, X. Sun, Microstructure, mechanical performance and anti-bacterial activity of degradable Zn-Cu-Ag alloy, Metals 12 (2022) 1444, https://doi.org/10.3390/met12091444.

[33] H. Jin, W. Li, L. Chen, Y. Lai, H. Guo, Q. Xing, X. Yang, Effects of Ag content and hot-rolling on microstructure and mechanical properties of Zn-Cu-xAg-Zr alloy, J. Mater. Eng. Perform. 31 (2022) 5964–5972, https://doi.org/10.1007/s11665-022-06661-3.

[34] J.Y. Lock, E. Wyatt, S. Upadhyayula, A. Whall, V. Nuñez, V.I. Vullev, H. Liu, Degradation and antibacterial properties of magnesium alloys in artificial urine for potential resorbable ureteral stent applications, J. Biomed. Mater. Res. Part A 102 (2014) 781–792, https://doi.org/10.1002/jbm.a.34741.

[35] E. Mostaed, M. Sikora-Jasinska, A. Mostaed, S. Loffredo, A.G. Demir, B. Previtali, D. Mantovani, R. Beanland, M. Vedani, Novel Zn-based alloys for biodegradable stent applications: Design, development and in vitro degradation, J. Mech. Behav. Biomed. Mater. 60 (2016) 581–602, https://doi.org/10.1016/j.jmbbm.2016.03.018.

[36] Clinical and Laboratory Standards Institute, Performance standards for antimicrobial disk susceptibility tests: Approved standard - Eleventh edition, 2012. https://doi.org/M02-A11.

[37] M. Balouiri, M. Sadiki, S.K. Ibnsouda, Methods for in vitro evaluating antimicrobial activity: A review, J. Pharm. Anal. 6 (2016) 71–79, https://doi.org/10.1016/j.jpha.2015.11.005.

[38] J. Jiang, H. Huang, J. Niu, Z. Jin, M. Dargusch, G. Yuan, Characterization of nano precipitate phase in an as-extruded Zn-Cu alloy, Scr. Mater. 200 (2021), https://doi.org/10.1016/j.scriptamat.2021.113907.

[39] J. Campbell, Complete Casting Handbook: Metal Casting Processes, Metallurgy, Techniques and Design: Second Edition, 2015. https://doi.org/10.1016/C2014-0-01548-1.

[40] H. Pal, S.K. Pradhan, M. De, Microstructural characterisation of hexagonal (Ag, Cu) Zn4 alloys in the deformed and as-cast state, Jpn. J. Appl. Phys. 33 (1994) 1443–1449, https://doi.org/10.1143/JJAP.33.1443.

[41] ASM International, ASM Handbook Volume 3: Alloy Phase Diagrams, 1998.

[42] D. Liu, W.A. Miller, K.T. Aust, Annealing twin formation in a cast and annealed Cu-4 at% Sn alloy, Can. Metall. Q 23 (1984) 237–240, https://doi.org/10.1179/cmq.1984.23.2.237.

[43] Robert E. Reed-Hill, Physical Metallurgy Principles, Van Nostrand,, 1973.

[44] S.R. Allahkaram, Technical note causes of catastrophic failure of high mn steel utilized as crusher overlaying shields, 2008. www.SID.ir.

[45] B. Mikulowski, B.R. Wielke, H.O.K. Kirchner, Anneal hardening of Zn and Zn-alloys, Acta Met. 30 (1982) 633–639, https://doi.org/10.1016/0001-6160(82)90112-2.

[46] Y. Zhang, Y. Yan, X. Xu, Y. Lu, L. Chen, D. Li, Y. Dai, Y. Kang, K. Yu, Investigation on the microstructure, mechanical properties, in vitro degradation behavior and biocompatibility of newly developed Zn-0.8%Li-(Mg, Ag) alloys for guided bone regeneration, Mater. Sci. Eng. C. 99 (2019) 1021–1034, https://doi.org/10.1016/j.msec.2019.01.120.

[47] C. Chen, S. Fan, J. Niu, H. Huang, Z. Jin, L. Kong, D. Zhu, G. Yuan, Alloying design strategy for biodegradable zinc alloys based on first-principles study of solid solution strengthening, Mater. Des. 204 (2021), 109676, https://doi.org/10.1016/j.matdes.2021.109676.

[48] C. Chen, J. Niu, H. Huang, D. Zhu, J.-F. Nie, G. Yuan, Basal-plane stacking fault energies of biodegradable Zn-based alloys: A first-principles study of alloying effects, Mater. Lett. 309 (2022), 131413, https://doi.org/10.1016/j.matlet.2021.131413.

[49] P. Kusakin, A. Belyakov, C. Haase, R. Kaibyshev, D.A. Molodov, Microstructure evolution and strengthening mechanisms of Fe-23Mn-0.3C-1.5Al TWIP steel during cold rolling, Mater. Sci. Eng. A. 617 (2014) 52–60, https://doi.org/10.1016/j.msea.2014.08.051.

[50] O. Bouaziz, S. Allain, C.P. Scott, P. Cugy, D. Barbier, High manganese austenitic twinning induced plasticity steels: A review of the microstructure properties relationships, Curr. Opin. Solid State Mater. Sci. 15 (2011) 141–168, https://doi.org/10.1016/j.cossms.2011.04.002.

[51] B.C. De Cooman, Y. Estrin, S.K. Kim, Twinning-induced plasticity (TWIP) steels, Acta Mater. 142 (2018) 283–362, https://doi.org/10.1016/j.actamat.2017.06.046.

[52] B.X. Huang, X.D. Wang, Y.H. Rong, L. Wang, L. Jin, Mechanical behavior and martensitic transformation of an Fe-Mn-Si-Al-Nb alloy, Mater. Sci. Eng. A. 438–440 (2006) 306–311, https://doi.org/10.1016/j.msea.2006.02.150.

[53] K.M.S. Youssef, C.C. Koch, P.S. Fedkiw, Improved corrosion behavior of nanocrystalline zinc produced by pulse-current electrodeposition, Corros. Sci. 46 (2004) 51–64, https://doi.org/10.1016/S0010-938X(03)00142-2.

[54] G. Ben-Hamu, D. Eliezer, K.S. Shin, S. Cohen, The relation between microstructure and corrosion behavior of Mg-Y-RE-Zr alloys, J. Alloy. Compd. 431 (2007) 269–276, https://doi.org/10.1016/j.jallcom.2006.05.075.

[55] N. Birbilis, K.D. Ralston, S. Virtanen, H.L. Fraser, C.H.J. Davies, Grain character influences on corrosion of ECAPed pure magnesium, Corros. Eng. Sci. Technol. 45 (2010) 224–230, https://doi.org/10.1179/147842209×12559428167805.
[56] M.C. Li, L.L. Jiang, W.Q. Zhang, Y.H. Qian, S.Z. Luo, J.N. Shen, Electrochemical corrosion behavior of nanocrystalline zinc coatings in 3.5% NaCl solutions, J. Solid State Electrochem 11 (2007) 1319–1325, https://doi.org/10.1007/s10008-007-0293-5.
[57] M. Wątroba, K. Mech, W. Bednarczyk, J. Kawałko, M. Marciszko-Wiąckowska, M. Marzec, D.E.T. Shepherd, P. Bała, Long-term in vitro corrosion behavior of Zn-3Ag and Zn-3Ag-0.5Mg alloys considered for biodegradable implant applications, Mater. Des. 213 (2022), 110289, https://doi.org/10.1016/j.matdes.2021.110289.
[58] H. Li, Y. Zheng, L. Qin, Progress of biodegradable metals, Prog. Nat. Sci. Mater. Int 24 (2014) 414–422, https://doi.org/10.1016/j.pnsc.2014.08.014.
[59] E. Mostaed, M. Sikora-Jasinska, J.W. Drelich, M. Vedani, Zinc-based alloys for degradable vascular stent applications, Acta Biomater. 71 (2018) 1–23, https://doi.org/10.1016/j.actbio.2018.03.005.
[60] C. García-Mintegui, L.C. Córdoba, J. Buxadera-Palomero, A. Marquina, E. Jiménez-Piqué, M.P. Ginebra, J.L. Cortina, M. Pegueroles, Zn-Mg and Zn-Cu alloys for stenting applications: From nanoscale mechanical characterization to in vitro degradation and biocompatibility, Bioact. Mater. 6 (2021) 4430–4446, https://doi.org/10.1016/j.bioactmat.2021.04.015.
[61] G. Katarivas Levy, J. Goldman, E. Aghion, The prospects of zinc as a structural material for biodegradable implants—a review paper, Metals 7 (2017) 402, https://doi.org/10.3390/met7100402.
[62] M. Schinhammer, J. Hofstetter, C. Wegmann, F. Moszner, J.F. Löffler, P. J. Uggowitzer, On the immersion testing of degradable implant materials in simulated body fluid: active pH regulation using CO 2, Adv. Eng. Mater. 15 (2013) 434–441, https://doi.org/10.1002/adem.201200218.
[63] M. Barbeck, T. Serra, P. Booms, S. Stojanovic, S. Najman, E. Engel, R. Sader, C. J. Kirkpatrick, M. Navarro, S. Ghanaati, Analysis of the in vitro degradation and the in vivo tissue response to bi-layered 3D-printed scaffolds combining PLA and biphasic PLA/bioglass components – Guidance of the inflammatory response as basis for osteochondral regeneration, Bioact. Mater. 2 (2017) 208–223, https://doi.org/10.1016/j.bioactmat.2017.06.001.
[64] G. Franci, A. Falanga, S. Galdiero, L. Palomba, M. Rai, G. Morelli, M. Galdiero, Silver nanoparticles as potential antibacterial agents, Molecules 20 (2015) 8856–8874, https://doi.org/10.3390/molecules20058856.
[65] X. Hong, J. Wen, X. Xiong, Y. Hu, Shape effect on the antibacterial activity of silver nanoparticles synthesized via a microwave-assisted method, Environ. Sci. Pollut. Res. 23 (2016) 4489–4497, https://doi.org/10.1007/s11356-015-5668-z.